




# Hollow porous nanocuboids cobalt-based metal–organic frameworks with coordination defects as anode for enhanced lithium storage

Juan-Juan Song<sup>1</sup>, Bin He<sup>1,2</sup>, Xinchao Wang<sup>2</sup>, Yueqi Guo<sup>2</sup>, Chunqing Peng<sup>2</sup>, Yang Wang<sup>1</sup>, Zhi Su<sup>2,\*</sup>, and Qingli Hao<sup>1,\*</sup> 

<sup>1</sup>Key Laboratory for Soft Chemistry and Functional Materials, Nanjing University of Science and Technology, 210094 Nanjing, China

<sup>2</sup>Key Laboratory of Biofunctional Materials, College of Chemistry and Materials Science, Nanjing Normal University, 210046 Nanjing, China

Received: 9 April 2021

Accepted: 13 July 2021

Published online:

22 July 2021

© The Author(s), under exclusive licence to Springer Science+Business Media, LLC, part of Springer Nature 2021

## ABSTRACT

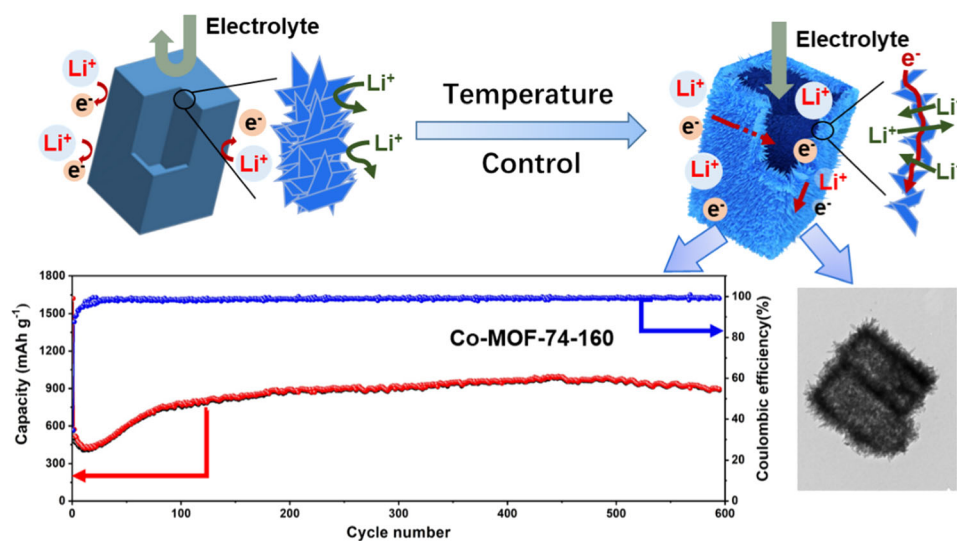
Controlling the morphology of metal–organic frameworks to improve their application in energy storage remains a particular challenge. In this work, hollow porous Co-MOF-74 nanocuboids consisting of nanothorn (< 7 nm) are designed through the linker exchange method for the improved MOFs-based anode of the lithium-ion battery. The Co-MOF-74 inherits the shape of cobalt acetate hydroxide prism and translates into the hollow structure due to the Kirkendall effect. The evolutions of morphology depending on temperature have been investigated further together with the lithium storage performances. Due to the combined merits from the high surface area inheriting from the nanocuboids and the coordination defects originating from the ultras-small nanothorns, the Co-MOF-74 with optimized morphology exhibits a high reversible capacity and excellent cycle stability (up to 900 mAh g<sup>-1</sup> at 1000 mA g<sup>-1</sup> after 600 cycles). This work demonstrates an effective way for rational design and synthesis of MOFs-based electrodes for energy storage.

Handling Editor: Mark Bissett.

Juan-Juan Song and Bin He have contributed equally to this work.

Address correspondence to E-mail: zhisu@njnu.edu.cn; qinglihao@njust.edu.cn

## GRAPHICAL ABSTRACT



## Introduction

Metal–organic frameworks (MOFs) have attracted numerous interests in many fields, such as catalysis, drug delivery, and gas separation because of their structural diversity, high surface area, tunable pores, etc. [1–4], especially in energy storage [5]. MOF has tunable pore and organic–inorganic hybrid properties; therefore, the direct fabrication of pure MOF-based LIB electrodes is becoming a rapidly growing field [6]. Early in 2006, Chen et al. [7] first reported MOF-177 as an anode material for LIBs. Subsequently, Gou et al. [8] reported  $\text{Co}_2(\text{OH})_2\text{BDC}$  as the anode electrode in LIBs, and the capacity of  $\text{Co}_2(\text{OH})_2\text{BDC}$  is  $650 \text{ mA h g}^{-1}$  at  $50 \text{ mA g}^{-1}$  after 100 cycles. Recently,  $\text{Ni-Me}_4\text{bpz}$  [9],  $\text{Cu}_3(\text{BTC})_2$  [10], and  $\text{Fe}(\text{Zn})\text{-BDC}$  [11] were also been studied as electrodes for energy storage and all of them show considerable electrochemical performance.

However, the poor conductivity of MOFs limits its application in lithium-ion battery [12]. Nowadays, functionalizing ligand and adding conductive carbon material are two main ways to improve the lithium storage performance of MOFs [13–15]. But only very few researches mention enhancing lithium storage properties from rational design morphology. Zhou

et al. [16] designed CPO-27 nanoarrays growing on Ni foams, which shows a reversible capacity of  $834 \text{ mAh g}^{-1}$  at  $50 \text{ mA g}^{-1}$ . What is important, recent studies have shown that hollow structure and ultrasmall nanoparticles can endow MOFs with improved properties. The hollow structure would distinctly heighten specific surface area and improve the rate of Li-ion migration<sup>14</sup>. And the ultrasmall MOFs exist coordination defects, which provided the more active sites [17, 18]. The electrochemical reaction kinetics can be improved obviously, leading to the improvement of the electrochemical performances. Many hollow MOFs and some ultrasmall MOFs have been reported [19, 20]. For example, Zhang et al. [21] reported a hollow MOF-74 with a dense outer wall and closed ends for  $\text{CO}_2$  separation, but the closed hollow structure is unfavorable for the diffusion of electrolyte in the cavity. The ultrasmall MOFs nanoparticles were synthesized by Xiao et al. [18] for the anode of lithium battery in 2018 with a capacity of  $1301 \text{ mAh g}^{-1}$  at  $0.1 \text{ A g}^{-1}$ . What is important, the linker exchange is a robust technique for synthesizing hollow MOFs [22]. However, the combination of hollow structure and ultrasmall MOFs nanoparticles has not yet been invested so much, and their applications in energy storage have not been widely reported [23].

Herein, we report a unique structure which is Co-MOF-74 hollow porous nanocuboids consisting of ultrasmall nanothorn ( $< 7$  nm) by linker exchange, and as anode for LIBs. The Co-precursor prism is firstly prepared through a reflux condensation method. Due to the differences in linker migration rate and regulation of nucleation rate, the solid Co source is gradually converted to hollow porous Co-MOF-74 during the ion-exchange process. The morphology of Co-MOF-74 is appropriately controlled by adjusting reaction temperature. Due to the combined advantages of high surface area, coordination defects, and multilevel porous, the optimized Co-MOF-74 electrode is conducive to lithium storage which exhibits a high reversible capacity ( $820 \text{ mAh g}^{-1}$  at  $1000 \text{ mA g}^{-1}$ ) and cycle stability ( $996 \text{ mAh g}^{-1}$  at  $1000 \text{ mA g}^{-1}$  after 470 cycles). This study introduces a novel design of hollow MOF structures with coordination defects for efficient lithium storage.

## Experimental section

### Synthesis of Co-precursor

PVP (1 g, MW  $\approx 58$  K) and cobalt acetate tetrahydrate (0.512 g, 2.056 mmol) were dissolved in ethanol (80 mL). Then, the mixed solution was added into the round-bottom flask to reflux under  $85^\circ\text{C}$  for 4 h; finally, the cobalt acetate hydroxide (Co-precursor) was collected following by washed with ethanol and dried in an oven at  $60^\circ\text{C}$ .

### Synthesis of Co-MOF-74-*x*

20 mg of cobalt acetate hydroxide was dispersed in 10 ml ethanol under sonication for 20 min, and then the 12 mg 2,5-dihydroxyterephthalic acid ( $\text{H}_4\text{Dobdc}$ ) was added into dispersion. The mixture solution was transferred into the autoclave and severally heated at 100, 120, 140, and  $160^\circ\text{C}$  for 24 h. The final products were collected and named as Co-MOF-74-*x* ( $x = 100, 120, 140, 160$ ).

### Characterizations

Powder X-ray diffraction (XRD) of Co-precursor and Co-MOF-74-*x* was conducted on Brooker D8 with  $\text{Cu K}\alpha$  radiation source as an X-ray diffractometer. The morphology of samples was represented by scanning

electron microscopy (SEM, Hitachi S-4800 scanning) and transmission electron microscope (TEM, JEOL JEM-2010F). The surface compositions of the samples were performed in X-ray photoelectron spectroscopy (XPS, Thermo VG Scientific ESCALAB 250 spectrometer). Barrett–Emmett–Teller (BET) surface area measurements were measured at Micromeritics ASAP 2050 instrument. The Fourier-transform infrared (FTIR) spectra were conducted on a Bruker Vector 22 FT-IR. The valence states were collected by a Thermo VG Scientific ESCALAB 250 spectrometer.

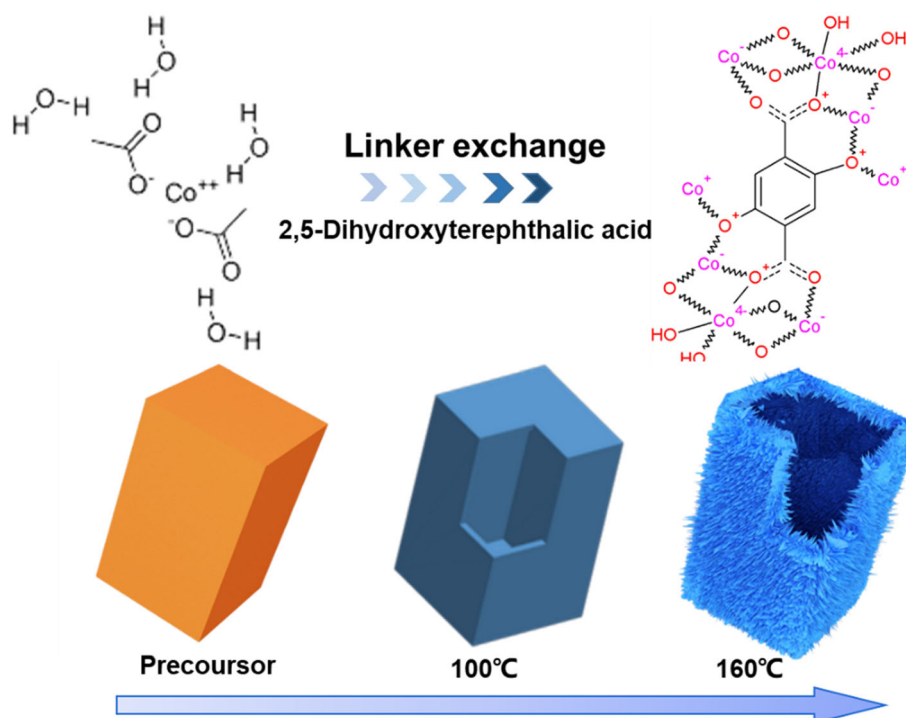
### Electrochemical measurements

The lithium storage performances of Co-MOF-74-*x* were examined by using CR2032 coin-type cells. The counter and the reference electrode, electrolyte, and separator are Li foils,  $\text{LiPF}_6$  (ethylene carbonate/dimethyl carbonate/dimethyl carbonate = 1: 1: 1 in volume), and Celgard 2400, respectively. The working electrode was composed of active material (70 wt%), conductive carbon black (20 wt%), and polyvinylidene fluoride (10 wt%). And then the slurry was coated on Cu foils and dried in a vacuum oven at  $105^\circ\text{C}$  for 10 h. The mass active mass load of the working electrode is between  $0.73 \sim 0.89$  mg. The charge and discharge measurements were conducted on the NEWARE battery station between 0.01 and 3.00 V at room temperature. Cyclic voltammetry (CV) curves were carried out by a CHI760C electrochemistry workstation with the voltage of 0.01–3 V. Electrochemical impedance spectroscopy (EIS) was conducted on CHI760D in the frequency range from 100,000 Hz to 0.1 Hz with an alternate current amplitude of 5 mV.

## Results and discussion

Scheme 1 demonstrates the preparation process of Co-MOF-74-*x*. Firstly, prism-shaped cobalt acetate hydroxide was prepared via oil bath by using surfactant PVP as a soft template. Subsequently, cobalt acetate hydroxide was selected as the Co source, while  $\text{H}_4\text{Dobdc}$  as organic ligand (permutoid) to synthesize Co-MOF-74-*x* by a facile solvothermal method. The molecular radius of  $\text{H}_4\text{Dobdc}$  is bigger than acetate, leading to the low migration rate for  $\text{H}_4\text{Dobdc}$  inside the material. Therefore, the  $\text{H}_4\text{Dobdc}$  will despoil and coordinate with cobalt in the surface

**Scheme 1** Schematic illustrating the preparation process of Co-MOF-74-160.



of cobalt acetate hydroxide due to coordination competition and differences in linker migration rate. The nucleation rate and molecular migration rate were significantly affected by the reaction temperature. Finally, the hollow porous Co-MOF-74-*x* consisting of nanothorns was controllably synthesized.

The crystal structures of the as-prepared Co-precursor and Co-MOF-74-*x* were revealed by XRD. As shown in Fig. 1a, the crystal structure of the Co-precursor is similar to the tetragonal cobalt acetate hydroxide phase (Co<sub>5</sub>(OH)<sub>2</sub>(CH<sub>3</sub>COO)<sub>8</sub>·2H<sub>2</sub>O) that

matches well with the standard data (JCPDS NO. 22–0582). After reacting with H<sub>4</sub>Dobdc under different reaction temperature, all the samples of Co-MOF-74-*x* show two broad peaks ~ 6.5° and 11.6°, which is consistent with the simulated peak pattern in a previously reported lecture [16]. What's more, the characteristic peaks of the Co-precursor are disappeared, which indicates that the synthesized material is exactly the Co-MOF-74-*x*. With the increase in reaction temperature, this peak shifts slightly, indicating the reduced space of crystal planes. Namely,

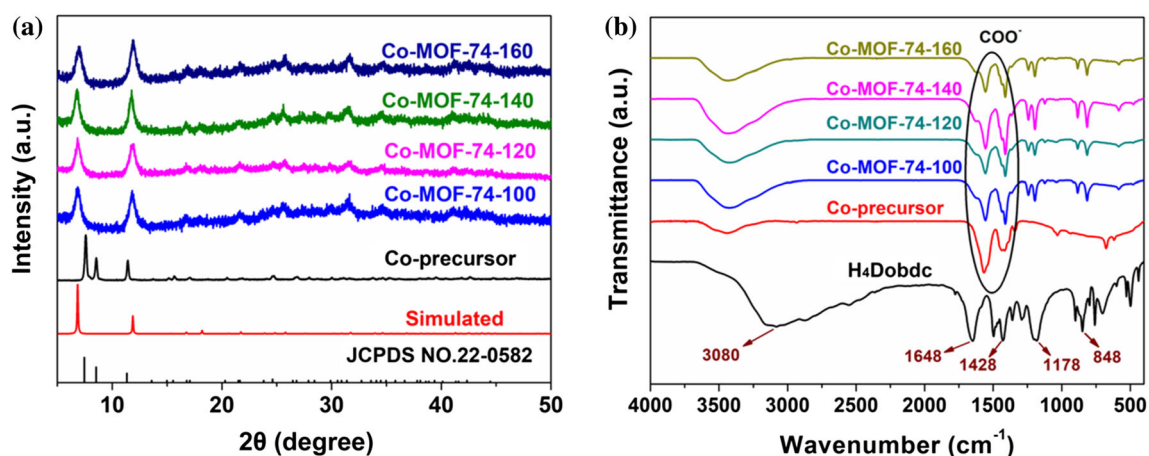


**Figure 1** a XRD pattern of the Co-precursor and Co-MOF-74-*x* and b FTIR spectra of Co-precursor, 2,5-dihydroxyterephthalic acid (H<sub>4</sub>Dobdc) and Co-MOF-74-*x*.

the high reaction temperature is equipped to contribute microscopic defects on these MOFs controllably meanwhile the overall structure was not excessively affected [24].

The FTIR spectra of Co-precursor, 2,5-dihydroxyterephthalic acid, and Co-MOF-74-*x* are compared in Fig. 1b. The absorption peak at 1178, 1428, and 3080  $\text{cm}^{-1}$  can be assigned to C–O, C=C ring, and O–H of non-ionized  $\text{H}_4\text{Dobdc}$  ligand, respectively [25]. For the Co-MOF-74-*x*, the characteristic absorption peak of the benzene ring out-of-plane vibration is also observed at 848  $\text{cm}^{-1}$ . The characteristic bands (O–H and C=O) of 2,5-dihydroxyterephthalic acid are changed obviously, which is caused by the formation of Co–O band between  $\text{Co}^{2+}$  and  $\text{H}_4\text{Dobdc}$  ligand. The FTIR spectras of Co-MOF-74-*x* are well consistent with the results reported in the literature [26]. The broadband at 3435  $\text{cm}^{-1}$  can be attributed to the C–O–H and interlayer  $\text{H}_2\text{O}$ . This suggests that Co from Co-precursors is successfully coordinated with the 2,5-dihydroxyterephthalic acid ligand.

As shown in Fig. 2a, the Co-precursor inherits a nanoprism structure with a smooth surface and uniform shape, which benefits from the soft template. The as-prepared Co-precursor was employed as the templates and reacted with  $\text{H}_4\text{Dobdc}$  through a solvothermal method to prepare Co-MOF-74-*x* samples.

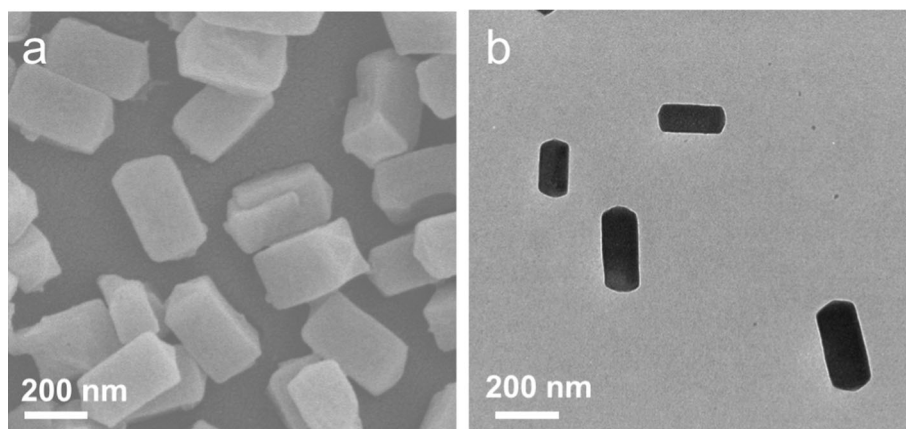
Compared with Co-precursor, a notable and disciplinary change in morphology was discovered on temperature-dependent reactions. The SEM images are presented in Fig. 3. The surface of the Co-precursors becomes rough, and nanothorns are grown on the entire surface of the Co-precursor. And the stuffed Co-precursors are gradually transformed into nanocubic and finally become hollow nanocubes with

openings at both ends. The Co-MOF-74-100 shows a microprism shape with a diameter of  $\sim 1 \mu\text{m}$  and a height of  $\sim 2 \mu\text{m}$ , consisting of nanothorn (Fig. 3a). The micromorphology of Co-MOF-74-100 was randomly dense, aggregated, and enclosed. The raised reaction temperature progressively led that the particle size of Co-MOF-74-120 (Fig. 3b) and Co-MOF-74-140 (Fig. 3c) decreased as well as the nanothorns. The morphology is gradually transformed to nanocuboids morphology with a diameter of  $\sim 0.5 \mu\text{m}$  and a height of  $\sim 1 \mu\text{m}$ . The inner diameter and the wall thickness of nanocuboids are  $\sim 150 \text{nm}$  and  $\sim 120 \text{nm}$ , respectively, as highlighted in the yellow lines in Fig. 3c. Finally, the Co-MOF-74-160 was completely transformed into nanocuboids with an inner diameter of 160 nm and a wall thickness of 70 nm as shown in Fig. 3d.

The formation of hollow structure can be briefly described as the following process. (i) The diameter of  $\text{H}_4\text{DOBDC}$  molecules is bigger than the channel of cobalt acetate hydroxide. (ii) The cobalt acetate hydroxide is transformed to MOF-74 from outside to inside. (iii) The Co atoms of cobalt acetate hydroxide are not enough to fill in the space of the original. (iv) Finally, the hollow MOF-74 particles were formed. Whereas the specific surface area and more active site of Co-MOF-160 are much higher than others, which facilitates contact between the electrolyte and electrode, the active sites provide more storage space for lithium ions and a more positive reaction. Interestingly, the wall got thinner and nanothorns become smaller as the reaction temperature increases because the nucleation rate and molecular migration rate all increase with the increase in temperature.

Figure 3e and f shows the TEM images of Co-MOF-160, hollow sea-urchin-like nanocuboids structure

**Figure 2** a SEM and b TEM images of the Co-precursor.



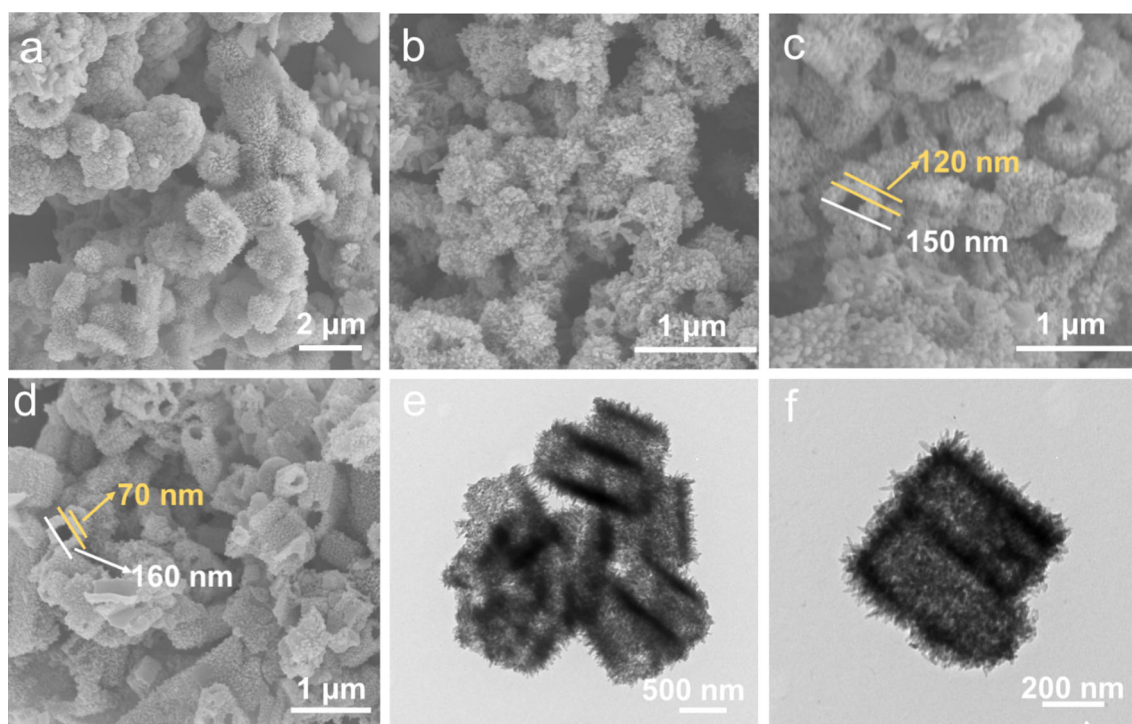


**Figure 3** SEM images of **a** Co-MOF-100, **b** Co-MOF-120, **c** Co-MOF-140, **d** Co-MOF-160 samples, and **e** and **f** TEM images of Co-MOF-74-160 sample.

can be observed, which is in good accord with the SEM results. The nanothorns with a width of  $\sim 7$  nm interconnects and generates highly porous nanocuboids. A light number of mesopores are observed in Fig. 3f. The porous hollow structure was conducive to promoting the diffusion of lithium ions in the Co-MOF-160 electrode and the intimate contact of nanothorns facilitated electron transfer, which is beneficial for the remarkable rate capability. What's more, the ultrasmall nanothorns would exist many coordination defects and lattice defects due to unsaturated coordination, which is more favorable for ion storage [27]. Therefore, the porous hollow Co-MOF-160 nanocuboids are favorable for Li-storage performance.

To further investigate the textural properties of the Co-MOF-160 electrode, the surface area and the pore-size distribution were measured by the nitrogen sorption analysis. The surface area calculated from the Brunauer–Emmett–Teller (BET) model is  $529.6 \text{ m}^2 \text{ g}^{-1}$ . The amount of  $\text{N}_2$  adsorption in the  $P/P_0 < 0.01$  region suggests the presence of micropores (Fig. 4a). And the hysteresis loop in the middle region proved the presence of mesoporous [28, 29]. From Fig. 4b, it can be observed that the pore

diameter is distributed at both micropores (1.7 nm) and mesopores (10–30 nm), demonstrating that Co-MOF-74-160 possesses a hierarchical pore, which facilitates the entry and storage of electrolyte.

The electronic structure and coordination environment of Co-MOF-74-160 were further analyzed by XPS (Fig. 5). The survey spectrum (Fig. 5a) indicates the existence of Co, C, and O elements. The peaks at binding energies of 797.3 and 781.4 eV belong to Co 2p<sub>1/2</sub> and Co 2p<sub>3/2</sub>. And the peaks at 802.3 and 785.8 eV are assigned to the satellite peaks [30]. The gap between Co2p<sub>1/2</sub> and Co 2p<sub>3/2</sub> is 15.9 eV, confirming that the  $\text{Co}^{2+}$  is the main existence form in Co-MOF-74-160 (Fig. 5b). The XPS spectrum of C 1s demonstrates three Gaussian peaks at 284.6 eV, 285.7 eV, and 288.5 eV corresponding to C–C, C=O, and O–C=O, respectively (Fig. 5c) [31]. The distinct peak of C–O species and the O 1s peak (Fig. 5d) located at 531.1, 531.8, and 533.15 eV could be ascribed to C–O–Co, C=O, and –O–H [32].

The lithium storage mechanism of MOF-74-160 was explored by CV in the range of 0.01–3.0 V at the scan rate of  $0.2 \text{ mV s}^{-1}$  (Fig. 6a). The first CV curve exhibits three cathodic peaks ( $\sim 1.58, 1.1,$  and  $0.58 \text{ V}$ ) corresponded to multistep lithiation of the organic

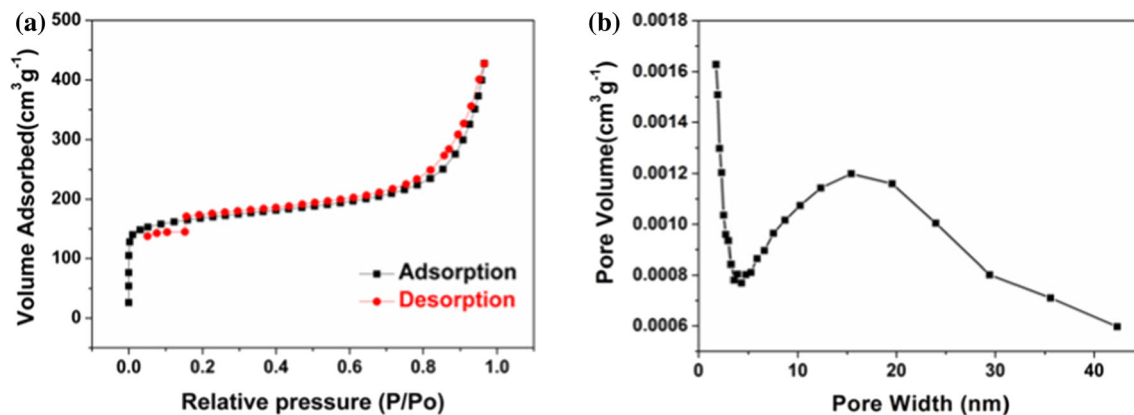


**Figure 4** a Nitrogen adsorption/desorption isotherm and b pore-size distribution of Co-MOF-160.

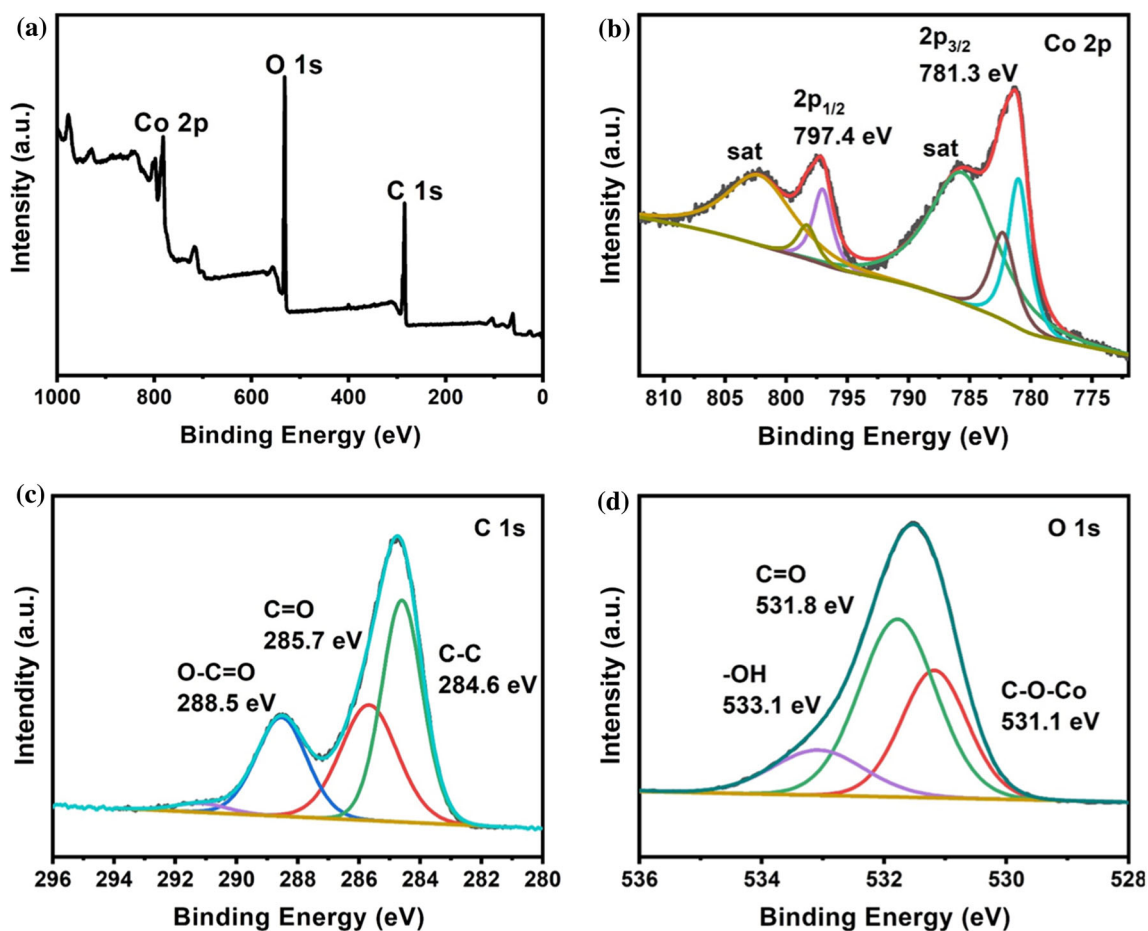


**Figure 5** XPS spectra of a survey spectra, b Co 2p, c C 1s, and d O 1s of Co-MOF-74-160 sample.

ligands including carboxylates and phenyl rings and the formation of SEI layer [33, 34], respectively. Meanwhile, two anodic peaks at 1.21 and 1.82 V are observed in the anode scan, which is attributed to the reversible delithiation of C=O and phenyl rings. A similar electrochemical reaction mechanism is also

proved by density functional theory in our group's previous work [35]. Compared with the first curves, the second CV curve changed. The peak intensity of both cathodic and anode gradually weakens and the peak position shifted slightly due to some irreversible reaction. The curves overlap well after 2 cycles, which

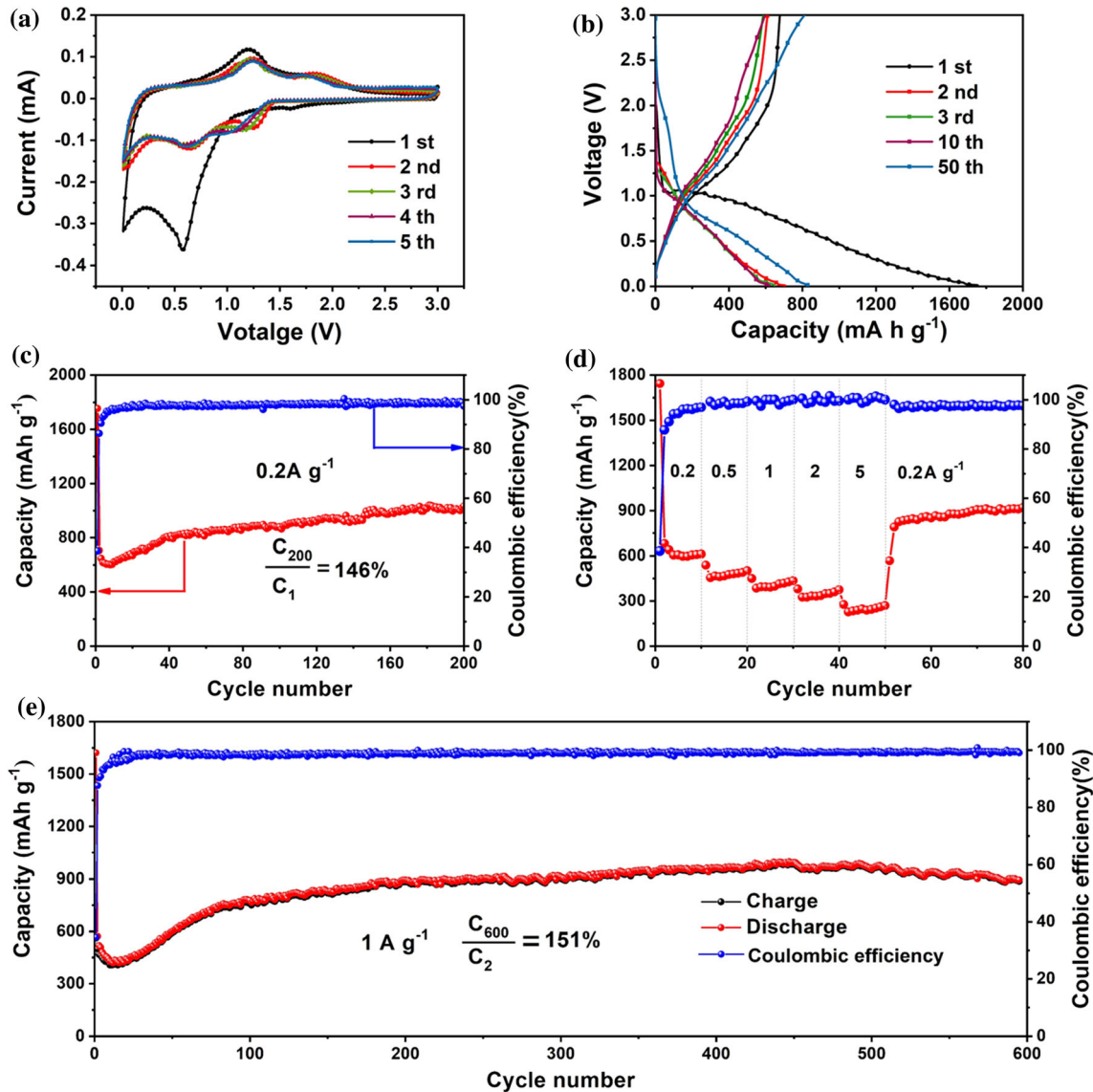


**Figure 6** **a** The first five CVs of the MOF-74-160 at a scan rate of  $0.2 \text{ mV s}^{-1}$  in the voltage range  $0.01\text{--}3.00 \text{ V}$  vs  $\text{Li}^+/\text{Li}$ ; **b** the first three, 10th, and 50th discharge/charge curves of MOF-74-160 at

$0.2 \text{ A g}^{-1}$ ; cycle performances of MOF-74-160 at  $0.2 \text{ A g}^{-1}$  (c) and at  $1 \text{ A g}^{-1}$  (e); rate performances and the corresponding Coulomb efficiency of MOF-74-160 at various rates (d).

indicates good reversibility of the electrochemical reactions [36].

The galvanostatic charge/discharge cycles are displayed in Fig. 6b. The first discharge (charge) specific capacity is  $2503 \text{ mAh g}^{-1}$  ( $972 \text{ mAh g}^{-1}$ ) with first Coulomb efficiency of 38%. The huge capacity fading in the first cycle is mainly attributed to the formation of solid electrolyte interface (SEI) layer [37] and the decomposition of electrolyte [30]; what more important is that some “dead active site” leads to the irreversible conversion reaction. The shape of lines almost overlaps the second one, indicating that Co-

MOF-160 has reversible electrochemical properties. And the Coulomb efficiency gradually increases and eventually approaches 100%. The profile was changed after 50 cycles that may be due to lithiation-induced reactivation and collapsing of large particles and aggregation of small particles.

The stable cycle performance of the MOF-74-160 electrode has been further investigated in LIBs; the cells were cycled for 200 cycles at  $0.2 \text{ A g}^{-1}$  and 600 cycles at  $1 \text{ A g}^{-1}$ , as presented in Fig. 6c, e. The MOF-74-160 electrode performs a high specific capacity of  $705 \text{ mA g}^{-1}$  (the second cycle) at a current density of



0.2 A g<sup>-1</sup>, and 571 mA g<sup>-1</sup> at 1 A g<sup>-1</sup>. The capacity experiences a steep fading, a rapid increase, and a slight increase whether at a high current density or a low current density. As shown in Fig. 6e, firstly, the capacity of MOF-74-160 gets 419 mA g<sup>-1</sup> (1 A g<sup>-1</sup>) at the 10th cycle and then displays 750 mA g<sup>-1</sup> at 80th cycle. Finally, the capacity increased to 970 mA g<sup>-1</sup> after 400 cycles and remained stable until the 600th cycle.

Basing on our experience results and the previous reports, the trend of decline followed by a rise may be put down to the following reasons. Firstly, the capacity decreases in the first several cycles, it may be caused by the incomplete lithium insertion reaction and the growth of SEI layers. During long-term cycling, the large porous nanocuboids undergo pulverization and gradually collapsed into smaller particles due to mechanical stress, leading to the increase in active sites. And, internal gradients of structure can result in a fracture that changes porosity; thus, it is easier for the electrolyte to participate in the reaction. Whether the increase in active sites or the changes of porosity, reaction kinetics will enhance, subsequently, the capacity will increase with cycling [35, 38].

The excellent electrochemical performance is also reflected in the multiplier rate properties. The rate performance at various current densities of MOF-74-160 is illustrated in Fig. 6d, the average specific capacities are approximately 606, 466, 393, 332, and 247 mA h g<sup>-1</sup> at 0.2, 0.5, 1, 2, and 5 A g<sup>-1</sup>, respectively, and the capacity increased to 839 mA h g<sup>-1</sup> when current densities returned 0.2 A g<sup>-1</sup>, suggesting the good reversibility of the Co-MOF-74-160 electrode. The Co-MOF-160 shows better stability and rate performance, which outperforms almost previously reported MOF-based electrodes (Table S1).

To further determine the effects of morphology on the electrochemical behaviors, Co-MOF-74-100, Co-MOF-74-120, and Co-MOF-74-140 were also chosen as the anode of LIBs. Figure 7a shows voltage profiles of Co-MOF-74-*x* electrodes for LIBs at 0.2 A g<sup>-1</sup>. With the higher active sites and surface area for the electrolyte to contact the electrodes, the prepared Co-MOF-74-160 electrode releases higher initial gravimetric discharge/charge capacities (2503/972 mA h g<sup>-1</sup>) than Co-MOF-74-100 electrode (1403 /545 mA h g<sup>-1</sup>), Co-MOF-74-120 electrode (1754/677 mA h g<sup>-1</sup>), and Co-MOF-74-140 electrode (1568 / 633 mA h g<sup>-1</sup>). The initial capacity increases with elevated reaction temperature.

In comparison, Co-MOF-74-100, Co-MOF-74-120, and Co-MOF-74-140 show poorer rate capability (Fig. 7b). The reversible capacity of Co-MOF-74-140 decreases from 514 to 244 mA h g<sup>-1</sup> with current densities increased from 0.1 to 5 A•g<sup>-1</sup>, respectively, and the capacity of Co-MOF-74-100 even drops to 88 mA h g<sup>-1</sup> at 5 A•g<sup>-1</sup>. It could be found that Co-MOF-74-160 shows higher discharge capacity whether in a high current or a low current, indicating that hollow porous MOF with defect groomed is an effective approach to improve the diffusion capability of Li-ions and enhance rate performance. The improved electrochemical performances can result from the abundant reaction sites provided by ultrasmall nanothorns and the effective lithium-ion diffusion provided by porous thin-walled nanocuboids as indicated in Fig. 7d.

Furthermore, compared with others, Co-MOF-74-160 also reveals a better capacity retention rate at a high current of 1 A g<sup>-1</sup> (Fig. 7c). During cycling, the large nanocubes Co-MOF-74-100/120/140 consisting of nanoparticles easily collapsed by the mechanical stress, and the nanoparticles would agglomerate, leading to attenuation of cycling performance. These results not only highlighted the favorable performance of nanocuboids Co-MOF-74-160, but also indicated that the reasonable morphology design of MOFs is a promising strategy for the application of lithium storage.

The EIS was conducted to further understand the electrochemical performances difference and estimate reaction kinetics of four materials. The Nernst plot of EIS consists of the charge transfer resistance ( $R_{ct}$ ) in high-frequency region and skew lines in low frequency, which are related to charge transfer resistance ( $R_{ct}$ ) and lithium-ion migration resistance ( $Z_w$ ), respectively. The  $R_{ct}$  of Co-MOF-74-*x* (*x* = 100, 120, 140 and 160) is 466, 288, 260, and 249 Ω cm<sup>-1</sup>, respectively. The  $R_{ct}$  decreases as the temperature increases, meaning that the Co-MOF-74-160 possesses the highest electrical conductivity. More importantly, the Co-MOF-74-160 exhibits the smallest  $Z_w$  among these four samples. The relatively low  $R_{ct}$  and  $Z_w$  of Co-MOF-74-160 elucidate the faster electrochemical reaction kinetics in comparison with another samples [39]. The ultrasmall nanothorns with defects would result in electronic reconfiguration and then enhance the charge transfer [40], which is more favorable for improving reaction kinetics and storing lithium ions.

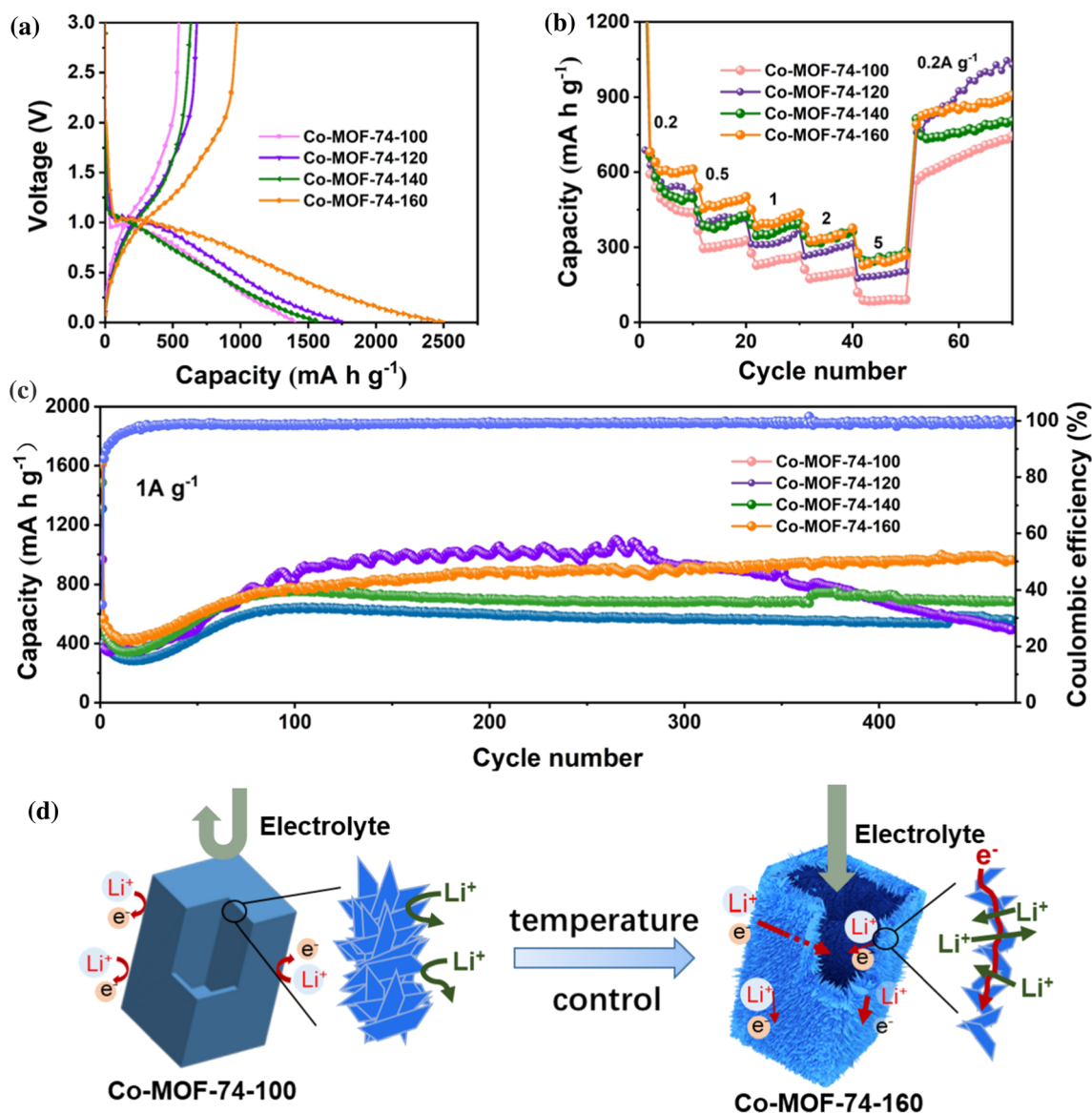


**Figure 7** **a** The first discharge/charge voltage profiles at 0.2 A g<sup>-1</sup>, **b** rate performance at various rates, **c** cycle performance at 1 A g<sup>-1</sup> of Co-MOF-74-*x* (*x* = 100, 120, 140 and 160), and **d** schematic illustration of improved ion/electron transport in Co-MOF-74-160.

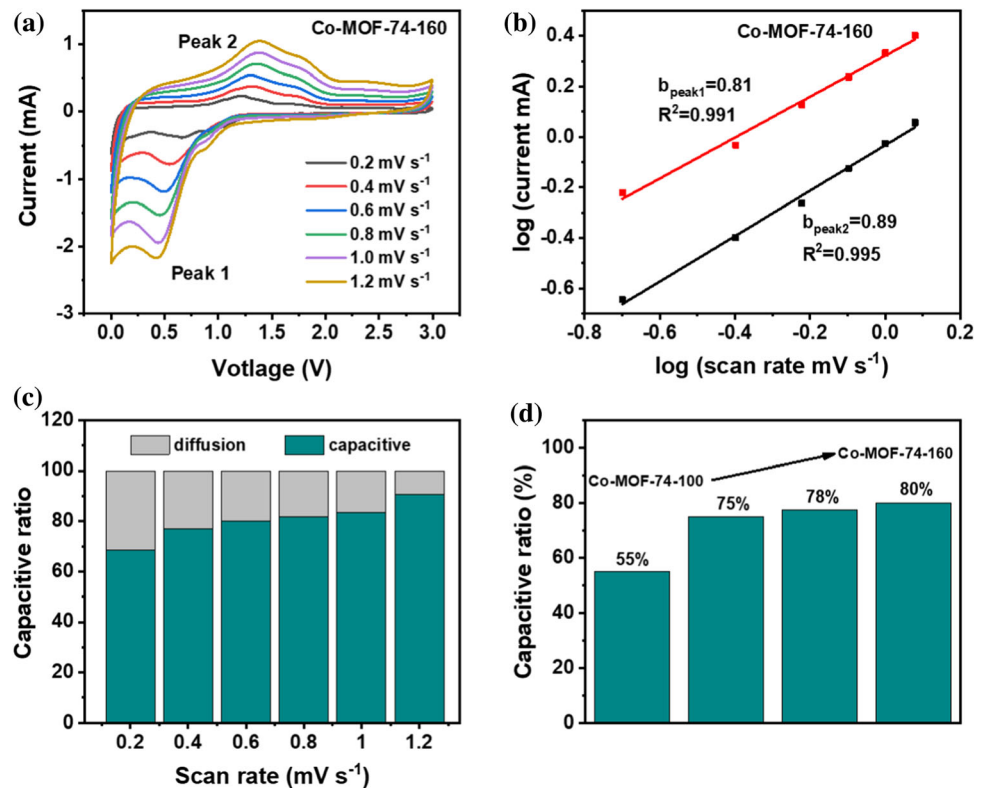
The CV with different scan rates (0.2–1.2 mV s<sup>-1</sup>) was also performed to further detect the charge storage mechanism (Fig. 8a). According to the equation of  $i = av^b$ , the linear relationships between log (scan rate) and log (peak current), the *b* value unravels that the lithium storage mechanism. As presented in Fig. 8b, the *b* value of Peak1 and Peak2 is 0.81 and 0.89, respectively, which elucidates the surface-dominated and the diffusion-dominated together contribution to the electrochemical reaction for Co-MOF-74-160 (Fig. 8b). As illustrated in Fig. 8c, the pseudocapacitive contribution is 68.5, 76.9, 80.0, 81.7, 83.3, and 90.7% at scan rate from 0.2 to 1.2 mV s<sup>-1</sup>,

respectively. The quantitative analyses indicate that the Co-MOF-74-160 electrode processes the highest pseudocapacitive contribution (Fig. 8d) and derived the conclusion that the Co-MOF-74-160 has favorable reaction kinetics and good rate capability.

## Conclusion

In conclusion, we have delicately designed and synthesized novel hollow nanocuboids Co-MOF-74 that consist of nanothorns directly as the anode for LIBs. The Co-precursor prism is firstly prepared through a

**Figure 8** **a** CV curves of Co-MOF-74-160 at different scan rates. **b** The linear relationship of  $\log$  (peak current) and  $\log$  (scan rate) of Co-MOF-74-160. The capacitive contributions of **c** Co-MOF-74-160 at different scan rates and **d** of Co-MOF-74- $x$  ( $x = 100, 120, 140$ , and  $160$ ) at the scan rate of  $0.6 \text{ mV s}^{-1}$ .



reflux condensation method and it subsequently becomes a Co source converted to form Co-MOF-74 by a facile ion-exchange method. The unique hollow nanocuboid with both open ends construction offers a high contact area between electrolyte and electrode, and the interconnected ultrasmall nanothorns provide fast channels for  $\text{Li}^+/\text{e}^-$  transport. Due to the synergy between the hollow nanocuboids morphology and interconnected ultrasmall nanothorns, the Co-MOF-74-160 can harvest an initial specific capacity of  $633 \text{ mA h g}^{-1}$  at a current density of  $1000 \text{ mA g}^{-1}$ , and gradually increases to  $970 \text{ mA h g}^{-1}$  after 400 cycles and keeps  $900 \text{ mA h g}^{-1}$  even after 500 cycles, indicating remarkable reversible capacity and cycle stability. Therefore, we believe that this attempt can be expanded research on hollow porous MOF materials using suitable precursor transform for energy storage.

## Acknowledgements

This work was supported by the National Natural Science Foundation of China (Nos. 51972173, 51872140), Program Foundation for Science and

Technology of Changzhou, China (CZ20190001), and the program for Science and Technology Innovative Research Team in Universities of Jiangsu Province.

**Supplementary Information:** The online version contains supplementary material available at <http://doi.org/10.1007/s10853-021-06341-y>.

## References:

- [1] He B, Xu C, Tang Y, Qian Y, Liu H, Hao Q, Su Z (2019) Facile fabrication of a hierarchical NiCoFeP hollow nanoprism for efficient oxygen evolution in the Zn-air battery. *J Mater Chem A* 7:24964–24972. <https://doi.org/10.1039/c9ta09239k>
- [2] Huang D, Liang C, Chen L, Tang M, Zheng Z, Wang Z (2021) MOF composite fibrous separators for high-rate lithium-ion batteries. *J Mater Sci* 56:5868–5877. <https://doi.org/10.1007/s10853-020-05559-6>
- [3] Jiao X, Hao Q, Xia X, Wu Z, Lei W (2019) Metal organic framework derived  $\text{Nb}_2\text{O}_5@\text{C}$  nanoparticles grown on reduced graphene oxide for high-energy lithium ion capacitors. *Chem Commun* 55:2692–2695. <https://doi.org/10.1039/c9cc00387h>

- [4] Zou L, Hou CC, Liu Z, Pang H, Xu Q (2018) Superlong single-crystal metal-organic framework nanotubes. *J Am Chem Soc* 140:15393–15401. <https://doi.org/10.1021/jacs.8b09092>
- [5] Jiang Y, Zhao H, Yue L, Liang J, Li T, Liu Q, Luo Y, Kong X, Lu S, Shi X, Zhou K, Sun X (2021) Recent advances in lithium-based batteries using metal organic frameworks as electrode materials. *Electrochem Commun*. <https://doi.org/10.1016/j.elecom.2020.106881>
- [6] Li C, Liu L, Kang J, Xiao Y, Feng Y, Cao F-F, Zhang H (2020) Pristine MOF and COF materials for advanced batteries. *Energ Storage Mater* 31:115–134. <https://doi.org/10.1016/j.ensm.2020.06.005>
- [7] Li X, Cheng F, Zhang S, Chen J (2006) Shape-controlled synthesis and lithium-storage study of metal-organic frameworks  $Zn_4O(1,3,5\text{-benzenetricarboxylate})_2$ . *J Power Sources* 160:542–547. <https://doi.org/10.1016/j.jpowsour.2006.01.015>
- [8] Gou L, Hao L-M, Shi YX, Ma S-L, Fan X-Y, Xu L, Li D-L, Wang K (2014) One-pot synthesis of a metal-organic framework as an anode for Li-ion batteries with improved capacity and cycling stability. *J Solid State Chem* 210:121–124. <https://doi.org/10.1016/j.jssc.2013.11.014>
- [9] An T, Wang Y, Tang J, Wang Y, Zhang L, Zheng G (2015) A flexible ligand-based wavy layered metal-organic framework for lithium-ion storage. *J Colloid Interface Sci* 445:320–325. <https://doi.org/10.1016/j.jcis.2015.01.012>
- [10] Maiti S, Pramanik A, Manju U, Mahanty S (2016)  $Cu_3(1,3,5\text{-benzenetricarboxylate})_2$  metal-organic framework: A promising anode material for lithium-ion battery. *Microporous Mesoporous Mater* 226:353–359. <https://doi.org/10.1016/j.micromeso.2016.02.011>
- [11] Lou X, Hu H, Li C, Hu X, Li T, Shen M, Chen Q, Hu B (2016) Capacity control of ferric coordination polymers by zinc nitrate for lithium-ion batteries. *RSC Adv* 6:86126–86130. <https://doi.org/10.1039/c6ra17608a>
- [12] Gao C, Jiang Z, Wang P, Jensen LR, Zhang Y, Yue Y (2020) Optimized assembling of MOF/SnO<sub>2</sub>/Graphene leads to superior anode for lithium ion batteries. *Nano Energy* 74:104868. <https://doi.org/10.1016/j.nanoen.2020.104868>
- [13] Mikita R, Ogihara N, Takahashi N, Kosaka S, Isomura N (2020) Phase transition mechanism for crystalline aromatic dicarboxylate in Li<sup>+</sup> intercalation. *Chem Mater* 32:3396–3404. <https://doi.org/10.1021/acs.chemmater.9b04984>
- [14] Wu Y, Zhao H, Wu Z, Yue L, Liang J, Liu Q, Luo Y, Gao S, Lu S, Chen G, Shi X, Zhong B, Guo X, Sun X (2021) Rational design of carbon materials as anodes for potassium-ion batteries. *Energ Storage Mater* 34:483–507. <https://doi.org/10.1016/j.ensm.2020.10.015>
- [15] Zhang C, Hu W, Jiang H, Chang J-K, Zheng M, Wu Q-H, Dong Q (2017) Electrochemical performance of MIL-53(Fe)@RGO as an Organic Anode Material for Li-ion Batteries. *Electrochim Acta* 246:528–535. <https://doi.org/10.1016/j.electacta.2017.06.059>
- [16] Zhou D, Ni J, Li L (2019) Self-supported multicomponent CPO-27 MOF nanoarrays as high-performance anode for lithium storage. *Nano Energy* 57:711–717. <https://doi.org/10.1016/j.nanoen.2019.01.010>
- [17] Wei R, Dong Y, Zhang Y, Zhang R, Al-Tahan MA, Zhang J (2020) In-situ self-assembled hollow urchins F-Co-MOF on rGO as advanced anodes for lithium-ion and sodium-ion batteries. *J Colloid Interface Sci* 582:236–245. <https://doi.org/10.1016/j.jcis.2020.08.044>
- [18] Xiao P, Bu F, Zhao R, Aly Aboud MF, Shakir I, Xu Y (2018) Sub-5 nm Ultrasmall Metal-Organic Framework Nanocrystals for Highly Efficient Electrochemical Energy Storage. *ACS Nano* 12:3947–3953. <https://doi.org/10.1021/acsnano.8b01488>
- [19] Feng L, Li J-L, Day GS, Lv X-L, Zhou H-C (2019) Temperature-controlled evolution of nanoporous MOF crystallites into hierarchically porous superstructures. *Chem* 5:1265–1274. <https://doi.org/10.1016/j.chempr.2019.03.003>
- [20] Qiu T, Gao S, Liang Z, Wang DG, Tabassum H, Zhong R, Zou R (2020) Pristine hollow metal-organic frameworks: design, synthesis and application. *Angew Chem Int Ed Engl* 60:2–25. <https://doi.org/10.1002/anie.202012699>
- [21] Zhang X, Chuah CY, Dong P, Cha YH, Bae TH, Song MK (2018) Hierarchically porous Co-MOF-74 hollow nanorods for enhanced dynamic CO<sub>2</sub> separation. *ACS Appl Mater Interfaces* 10:43316–43322. <https://doi.org/10.1021/acsami.8b17180>
- [22] Dodson RA, Kalenak AP, Matzger AJ (2020) Solvent choice in metal-organic framework linker exchange permits microstructural control. *J Am Chem Soc* 142:20806–20813. <https://doi.org/10.1021/jacs.0c10224>
- [23] Fan M, Liao D, Aboud MFA, Shakir I, Xu Y (2020) A universal strategy toward ultrasmall hollow nanostructures with remarkable electrochemical performance. *Angew Chem Int Ed Engl* 59:8247–8254. <https://doi.org/10.1002/anie.202000352>
- [24] Zheng X, Jia G, Fan G, Luo W, Li Z, Zou Z (2020) Modulation of disordered coordination degree based on surface defective metal-organic framework derivatives toward boosting oxygen evolution electrocatalysis. *Small* 16:e2003630. <https://doi.org/10.1002/sml.202003630>
- [25] Liao Y, Li C, Lou X, Wang P, Yang Q, Shen M, Hu B (2017) Highly reversible lithium storage in cobalt 2,5-dioxido-1,4-benzenedicarboxylate metal-organic frameworks boosted by

- pseudocapacitance. *J Colloid Interface Sci* 506:365–372. <https://doi.org/10.1016/j.jcis.2017.07.063>
- [26] Zhao X, Pattengale B, Fan D, Zou Z, Zhao Y, Du J, Huang J, Xu C (2018) Mixed-node metal-organic frameworks as efficient electrocatalysts for oxygen evolution reaction. *ACS Energy Lett* 3:2520–2526. <https://doi.org/10.1021/acsenerylett.8b01540>
- [27] Yue L, Ma C, Yan S, Wu Z, Zhao W, Liu Q, Luo Y, Zhong B, Zhang F, Liu Y, Alshehri AA, Alzahrani KA, Guo X, Sun X (2021) Improving the intrinsic electronic conductivity of NiMoO<sub>4</sub> anodes by phosphorous doping for high lithium storage. *Nano Res*. <https://doi.org/10.1007/s12274-021-3455-3>
- [28] Yao D, Wang F, Lei W, Hua Y, Xia X, Liu J, Hao Q (2020) Oxygen vacancies boosting ultra-stability of mesoporous ZnO-CoO@N-doped carbon microspheres for asymmetric supercapacitors. *Science China-Materials* 63:2013–2027. <https://doi.org/10.1007/s40843-020-1357-9>
- [29] Xi G, Jiao X, Peng Q, Zeng T (2021) Anchored CoCO<sub>3</sub> on peeled graphite sheets toward high-capacity lithium-ion battery anode. *J Mater Sci* 56:10510–10522. <https://doi.org/10.1007/s10853-021-05933-y>
- [30] Nagaraju G, Sekhar SC, Ramulu B, Hussain SK, Narsimulu D, Yu JS (2020) Ternary MOF-based redox active sites enabled 3d-on-2d nanoarchitected battery-type electrodes for high-energy-density supercapacities. *Nano-Micro Letters* 13:17. <https://doi.org/10.1007/s40820-020-00528-9>
- [31] Ouyang Y, Huang R, Xia X, Ye H, Jiao X, Wang L, Lei W, Hao Q (2019) Hierarchical structure electrodes of NiO ultrathin nanosheets anchored to NiCo<sub>2</sub>O<sub>4</sub> on carbon cloth with excellent cycle stability for asymmetric supercapacitors. *Chem Eng J* 355:416–427. <https://doi.org/10.1016/j.cej.2018.08.142>
- [32] Aminu IS, Geaney H, Imtiaz S, Adegoke TE, Kapuria N, Collins GA, Ryan KM (2020) A copper silicide nanofoam current collector for directly grown Si nanowire networks and their application as lithium-ion anodes. *Adv Func Mater* 30:2007238. <https://doi.org/10.1002/adfm.202003278>
- [33] Bi R, Xu N, Ren H, Yang N, Sun Y, Cao A, Yu R, Wang D (2020) A hollow multi-shelled structure for charge transport and active sites in lithium-ion capacitors. *Angew Chem Int Ed Engl* 59:4865–4868. <https://doi.org/10.1002/anie.201914680>
- [34] Mutahir S, Wang C, Song J, Wang L, Lei W, Jiao X, Khan MA, Zhou B, Zhong Q, Hao Q (2020) Pristine Co(BDC)TED<sub>0.5</sub> a pillared-layer biligand cobalt based metal organic framework as improved anode material for lithium-ion batteries. *Appl Mater Today* 21:100813. <https://doi.org/10.1016/j.apmt.2020.100813>
- [35] Ding Y, Hu L, He D, Peng Y, Niu Y, Li Z, Zhang X, Chen S (2020) Design of multishell microsphere of transition metal oxides/carbon composites for lithium ion battery. *Chem Eng J* 380:122489. <https://doi.org/10.1016/j.cej.2019.122489>
- [36] Gong F, Xia D, Li M, Zhou Q, Wang D, Zhang P, Zhang Y (2020) Direct thermal pyrolysis enabling the use of cobalt oxides nanoparticles from commercial acetates as high-capacity anodes for lithium-ion batteries. *Ind Eng Chem Res* 59:13564–13571. <https://doi.org/10.1021/acs.iecr.0c01895>
- [37] Shan Y, Li Y, Pang H (2020) Applications of tin sulfide-based materials in lithium-ion batteries and sodium-ion batteries. *Adv Func Mater* 30:2001298. <https://doi.org/10.1002/adfm.202001298>
- [38] Zhao W, Gao L, Yue L, Wang X, Liu Q, Luo Y, Li T, Shi X, Asiri AM, Sun X (2021) Constructing a hollow microflower-like ZnS/CuS@C heterojunction as an effective ion-transport booster for an ultrastable and high-rate sodium storage anode. *Journal of Materials Chemistry A* 9:6402–6412. <https://doi.org/10.1039/d1ta00497b>
- [39] Zheng X, Jia G, Fan G, Luo W, Li Z, Zou Z (2020) Modulation of disordered coordination degree based on surface defective metal-organic framework derivatives toward boosting oxygen evolution electrocatalysis. *Small* 16:2003630. <https://doi.org/10.1002/sml.202003630>

**Publisher's Note** Springer Nature remains neutral with regard to jurisdictional claims in published maps and institutional affiliations.